Available online at www.sciencedirect.com

ScienceDirect

Advances in Space Research 62 (2018) 2199–2212

ADVANCES IN SPACE RESEARCH (a COSPAR publication)

www.elsevier.com/locate/asr

Anticipated electrical environment at Phobos: Nominal and solar storm conditions

W.M. Farrell [a,*], J.S. Halekas [b], S. Fatemi [c], A.R. Poppe [c], C. Hartzell [d], J.R. Marshall [e], T.J. Stubbs [a], M.I. Zimmerman [f], Y. Zheng [a]

[a] NASA Goddard Space Flight Center, Greenbelt, MD 20771, USA
[b] University of Iowa, Iowa City, IA 52242, USA
[c] University of California at Berkeley, Berkeley, CA 94720, USA
[d] University of Maryland, College Park, MD 20742, USA
[e] SETI Institute, Mountain View, CA 94043, USA
[f] Johns Hopkins University/Applied Physics Laboratory, Laurel, MD 20723, USA

Received 28 January 2017; received in revised form 1 August 2017; accepted 8 August 2017
Available online 5 September 2017

Abstract

A passing coronal mass ejection (CME) will manifest a different response at an airless body compared to a magnetized planet. Specifically, because the regolith-rich surfaces of airless bodies are directly exposed to the variations in the plasma flow, the surfaces are found to undergo anomalous surface charging during the passing of CME fast plasma events. In this study, we model the surface charging expected at Phobos for nominal solar wind conditions and also those associated with disturbed solar wind conditions during the passage of a CME similar to that observed by MAVEN at Mars in early March 2015. We use an ambipolar diffusion model to examine the development of the trailing wake/void in the plasma flow behind Phobos and the formation of mini-wakes within obstruction regions like Stickney Crater. We also consider the roving of an astronaut in Stickney Crater for Phobos positioned near 10 h Local Time relative to Mars. We examine the plasma dissipation of the collected astronaut charge from contact electrification with the regolith.

Keywords: Mars; Phobos; Surface charging

1. Introduction

It is well known that exposed surfaces immersed in plasmas will charge to reach a balance of species flux. This process has been well-studied for the Moon (for example, Manka (1973), Halekas et al. (2011), Stubbs et al. (2014) and references therein) and there is now a new appreciation of this plasma-induced surface charging for other exposed rocky bodies throughout the solar system. In this work, we consider the plasma interaction at Mars' moon Phobos to both understand where and when charging can be extreme and to also understand the effect the plasma environment has on the charged state of any human surface explorer.

Fig. 1 (adapted from Jackson et al., 2015) illustrates the charging environment at an exposed body (Earth's Moon) and represents an example of expectations for Phobos in the solar wind. On the dayside, solar UV radiation liberates electrons from the surface, creating a photo-electron current ($\sim$4 $\mu A/m^2$) (Feuerbacher et al., 1972) that exceeds the solar wind electron thermal flux ($\sim$1.5 $\mu A/m^2$) and solar wind ion inflow ($\sim$0.3 $\mu A/m^2$). Consequently, the surface charges a few volts positive (Poppe and Horanyi, 2010), which acts to electrically-trap most of the low energy

* Corresponding author.
E-mail address: william.m.farrell@nasa.gov (W.M. Farrell).

https://doi.org/10.1016/j.asr.2017.08.009
0273-1177/Published by Elsevier Ltd on behalf of COSPAR.

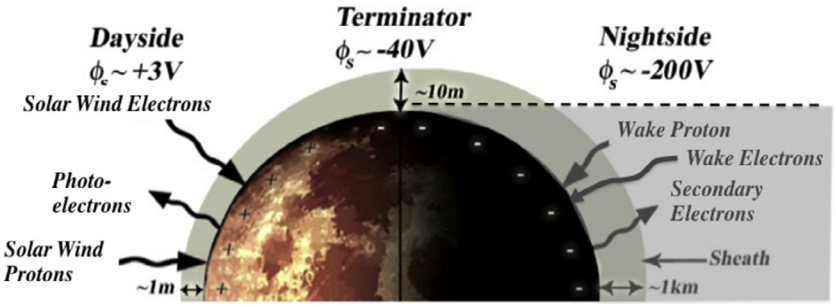

Fig. 1. An illustration of the surface potential across a large airless body (in this case, the Moon) showing the positive potentials on the lunar dayside and large negative potentials that develop in shadowed regions. Adapted from Jackson et al. (2015).

photo-electrons to a near-surface sheath of about 0.5 to 1 meter in size. Local current balance is then maintained by the return flux of trapped photo-electrons. See Figure 3 of Stubbs et al. (2014) which shows currents at the lunar surface as a function of solar zenith angle. Zakharov et al. (2014) also discussed the currents and sheaths expected at Phobos, from a global and local perspective.

During solar storms, the solar wind electron thermal flux can become large (>4 $\mu A/m^2$) and, in doing so, effectively reduces the trapping surface potential - which then allows the release of a larger fraction of photo-electrons into upstream regions (Farrell et al., 2013).

As suggested in the figure, in shadowed regions beyond the terminator, the surface potential becomes increasingly negative with increasing solar zenith angle. This effect occurs because the collisionless solar wind flowing past the body at nominally 400 km/s creates a trailing void or wake region behind the Moon that gets filled in via thermal expansion, plasma gyration, and ambipolar diffusion processes (Crow et al., 1975; Samir et al., 1983; Ogilvie et al., 1996; Halekas et al., 2005). This ambipolar process limits the electron and ion currents that reaches the anti-solar point. This wake expansion region extends behind the object for a substantial distance (illustrated shaded region). Consequently, the surface charges strongly negative since the electron thermal flux greatly exceeds that of the ions. This strong negative potential (to many hundreds of volts) will repel electrons to maintain flux balance. The enhanced nightside negative surface charging has been verified via direct observation from the Lunar Prospector Magnetometer/Electron Reflectometer (Mag/ER) instrument (see Figure 3 of Halekas et al., 2011). Only the most energetic solar wind electrons can propagate deep into the wake region behind the Moon. Their incidence at the surface also releases secondary electrons which remediate excessive charge build-ups (see the discussion in Halekas et al., 2011) and these are also labeled in the figure.

While Fig. 1 illustrates the global plasma-surface interaction, there can be profound regional charging effects around complicated topography at the terminator boundary (Farrell et al., 2010; Zimmerman et al., 2011, 2012, 2013). Fig. 2 is a cartoon illustration of the horizontally-flowing solar wind past a crater located at the terminator

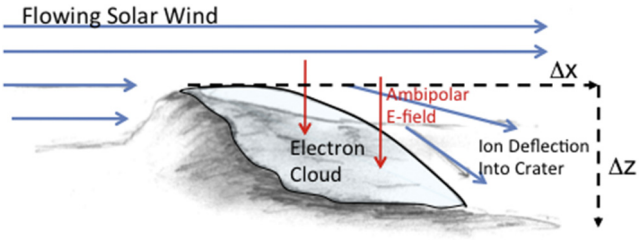

Fig. 2. The ambipolar expansion of solar wind plasma into a void formed by an obstacle. Illustrated is a crater at the terminator. The initially-horizontally flowing solar wind gets deflected into regions behind the crater by the formation of an ambipolar E-field.

region of any airless body. The ambipolar process is 'self-similar' in that it scales as the ratio of the ion sound speed-to-solar wind speed, C_s/V_{sw}. Consequently, an ambipolar E-field and diffusion process is initiated immediately downstream and around local topography that allows the solar wind to expand back into the initial void region.

In essence, the plasma expansion into a void is initiated by the low mass electrons, which propagate into the void ahead of the more massive ions. This separation creates an ambipolar E-field that electrostatically defects the solar wind ion flow at 400 km/s into the void. On the leeward edge of the solar wind inflow, the ions have difficulty being deflected to the surface and there is the development of an 'electron cloud' (Crow et al., 1975; Farrell et al., 2008; Zimmerman et al., 2011) with an electron-rich plasma forming. If a roving object tribo-charges to negative potentials, the lack of ions in this electron-rich cloud region would lead to long dissipation charge times that can be of concern for explorers. This issue will be described more in Section 6.

As an example, Figure 2 of Jackson et al., 2011 shows the anticipated surface potential and ion current expected at the bottom of Shoemaker crater at the Moon from an ambipolar diffusion and surface charging code (Farrell et al., 2010; Jackson et al., 2011). This model is similar to that applied herein for Phobos (see Section 4 for more description). The development of large negative potentials and low ion currents along the leeward edge of the crater are indicative of the difficulty in electrostatically-diverting

ions along this leeward crater wall region. This figure shows the typical output from the ambipolar codes, providing both an estimate of potential relative to the solar wind and an estimate of inflowing ion and electron current to the surface. We now present the application of these same codes for Mars moon Phobos to examine the plasma-surface electrical interaction and to determine regions where plasma flow will become electrically complex.

2. An Introduction to the 'the space environment in Stickney crater' study

The work herein represents a portion of a larger effort from over 30 investigators who are part of the Dynamic Response of the Environments at Asteroids, the Moon, and moons of Mars (DREAM2) Center for Space Environments (http://ssed.gsfc.nasa.gov/dream/). DREAM2 is a node of the parent organization Solar System Exploration Research Virtual Institute (SSERVI) that has the objective to connect the latest scientific understandings of the Moon, asteroids, and moons of Mars to human exploration – in close support of exploration.

In 2015–2016, the DREAM2 team undertook a systematic study of the space environment at Phobos, including the development of plasma, exosphere, and surface interaction models, run in sequence and in common space environment conditions to understand the effect the radiation, space plasma, and micro-meteoroid environment has at this exposed irregularly-shaped ~22 km body. The title of this intramural study is the 'Space Environment in Stickney Crater (SEinSC)' that addressed the space environment at Phobos. Stickney crater was targeted as an ideal regional-scale feature for examination. We present results from the space plasma–moon interaction herein, with other papers in this special issue also part of this larger team-level study.

Specifically, the SEinSC study used inputs from the Mars Atmosphere and Volatile Evolution (MAVEN) mission (Jakosky et al., 2015a,b), models of the inner heliospheric solar wind from the Community Coordinated Modeling Center (CCMC, see (http://ccmc.gsfc.nasa.gov)), University of New Hampshire radiation propagation models (http://emmrem.unh.edu), and data from the Virtual Energetic Particle Observatory (https://vepo.gsfc.nasa.gov). These contextual data sets were used as inputs to the detailed tactical DREAM2 models such as hybrid plasma simulations of the Mars-solar wind interaction, kinetic models of the Phobos-plasma interactions, neutral gas and photo-ion models, radiation-induced deep dielectric discharge models, and radiation/human effect modeling. Impact gardening and solar illumination/temperature models of Phobos were also developed to examine volatile retention and longevity. Models of solar wind hydroxylation at Phobos were also developed to better understand the previous observations of a 2.8 μm absorption feature in the NIR spectra from a possible OH veneer (Fraeman et al., 2014). Possible Phobos missions that might provide validation or further context of the SEinSC findings were also discussed.

3. Mars space plasma environment applied in this study

The SEinSC study was performed at an ideal time when the Martian magneto-plasma environment was being revealed in stunning new detail by the Mars Atmosphere and Volatile Evolution (MAVEN) mission. The MAVEN payload included electron and ion spectrometers, ion composition system, neutral mass spectrometer, a magnetometer, Langmuir probe, high energy particle telescope and imaging UV spectrometer instrumentation (Jakosky et al., 2015c). The mission was launched on 10 November 2013 and placed into Mars orbit on 21 September 2014 in a 150 km × 6200 km orbit inclined at 74°. Phobos, orbiting at ~2.76 R_M about Mars, thus passes through a set of key plasma boundaries every ~7.65 h that were also examined by MAVEN (see Jakosky et al., 2015a,b and references therein). The SEinSC study was greatly enabled by the timing of the MAVEN program's release of science results to the public.

Figure 7 of Jakosky et al., 2015b shows the average MAVEN-measured plasma properties relative to the locations of the Martian bow shock, magnetosheath, and ionosphere-magnetosphere boundary (IMB). Specifically, for Phobos orbiting at 2.76 R_M, its spends part of its orbit in upstream regions in the undisturbed solar wind, but the moon also is immersed in plasma originating from Mars as it passes through the Mars tail region. Fig. 3 shows the expected plasma density and velocity in the near-Mars environment and under nominal solar wind conditions (~3 cm^{-3}, ~400 km/s) derived from a hybrid simulation developed by S. Fatemi (published in Poppe et al., 2016). The simulation is for an interplanetary magnetic field (IMF) that points mostly out of the ecliptic, but the case for B in the ecliptic plane is similar (Poppe et al., 2016). The dashed circle about Mars represents the orbit of Phobos. From a density perspective, the moon is in nominal solar wind from a Martian local time of 6 to 18 h. However, near 18 h LT, the moon cross the bow shock and enters into the higher density magnetosheath region consisting of a warm, high density plasma of >10 cm^{-3} of about 2 R_M in width. Thereafter, the moon cross the IMB and then enters a lower density plasma in the magnetic tail region from hour 20 to hour 4 LT. This tail plasma propagating away from Mars consists of energetic heavy ions (like O^+) originating from Mars itself. Between 0 and 4 h LT, the hybrid simulations modeling kinetic ion particles and fluid electrons indicate that the plasma has slowed to below 300 km/s at Phobos distances. We note that this slowdown in this region is strongly IMF dependent and the situation would change for a different IMF configuration. Near 4 h LT, the moon again crosses the IMB to enter into the magnetosheath and at 6 h LT crosses the bow shock and again enters the solar wind plasma.

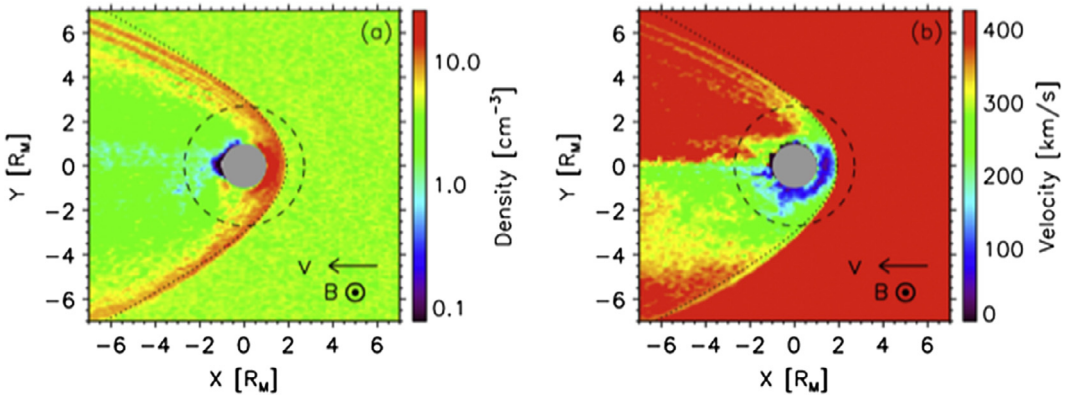

Fig. 3. Shown are the plasma density and velocity in the near-Mars environment derived from a plasma hybrid simulation (adapted from Poppe et al., 2016). Solar wind is inflowing from right to left, and altered by Mars. This model shows the formation of a bow shock, a higher density, warmer magnetosheath, and a separate Martian plasma tail. The orbit of Phobos at 2.76 RM is identified as the dashed-line about Mars. During its ~7.65 h orbit, Phobos passes through all three plasma regimes: undisturbed solar wind, magnetosheath and magnetic tail plasma.

The MAVEN spacecraft has been in orbit about Mars since September 2014, and observed the passage of a substantial solar storm past the planet in early March 2015 (Jakosky et al., 2015a). For this study of Phobos, we use observations from this event as initial conditions for our models.

Before the arrival of the 8 March 2015 CME, the nominal solar wind flow as measured by MAVEN (and applied to our model herein) had a density of $n_{sw} = 2.4/cm^{-3}$, flow speed of $v_{sw} = 370$ km/s, electron temperature of $T_e = 7.5$ - eV, and ion temperature of $T_i = 5.5$ eV. The magnetic field during this pre-storm period is ~3 nT oriented in the ecliptic plane. However, during the passing of the warm sheath of a CME during the 8 March 2015 solar storm, these MAVEN-measured values near 16:35 UT changed to $n_{sw} = 2.7/cm^3$, $V_{sw} = 832$ km/s, $T_e = 33$ eV, $T_i = 88$ eV, B = 12 T, with the field directed about 45° out of the ecliptic plane. Figure 2 of Jakosky et al. (2015a) shows the evolution of MAVEN-measured near-Mars plasma during the 8 March 2015 CME passage event.

Fig. 4 provides context on the solar storm/CME activity occurring during this early March 2015 period. Shown is an MHD model of the disturbed plasma emitted from the sun as provided by the Community Coordinated Modeling Center (see further description of model in figure caption). Specifically, an active region on the sun was releasing energetic plasma coronal mass ejections (CMEs) into the inner heliosphere nearly quasi-periodically every 2 days. An ejection event was launched in early 6 March 2016 that then pass by the Mars-Phobos system on 8 March, and during an approximate 20 h period the solar wind at the Mars-Phobos system became disturbed. Jakosky et al. (2015a) point out that the 8 March event was actually two separate solar ejection events that merged.

Given the driving conditions at Mars, we can run hybrid simulations addressing the effect the solar storm has on the Martian plasma environment. Fig. 5 shows a hybrid simulation result displaying the plasma environment along the

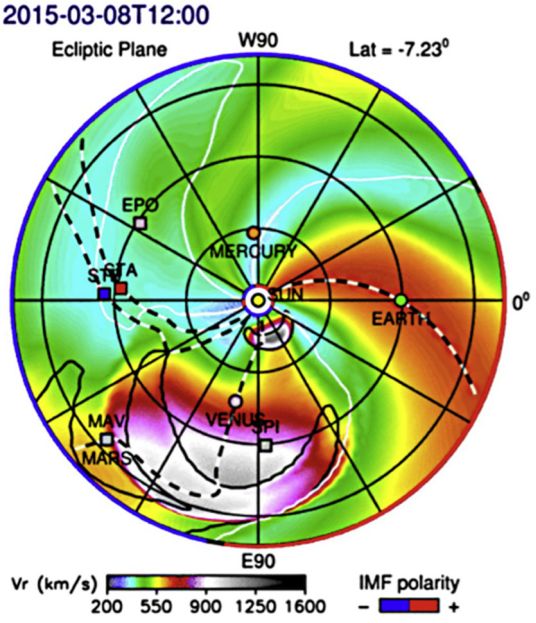

Fig. 4. The Wang-Sheeley-Arge (WSA) –ENLIL + Cone model (Mays et al., 2015) for mapping the transit of coronal mass ejections through the inner heliosphere. The model is run for the case of a 6 March 2015 solar disturbance, which passes by Mars (lower left hand corner) on 8 March.

Phobos orbital path for both nominal and solar storm-like conditions (using the code developed by S. Fatemi as in Fig. 3). In the figure, the location of 180° in orbital phase is the anti-sunward location (24 Hr Local Time). While the solar wind and magnetosheath region contain solar wind plasma, the magnetic tail of Mars contains mostly ions of Mars origin, like O^+ (Poppe et al., 2016). As indicated in the figure, under the increase pressure of the solar wind, the tail region near 2.76 R_M becomes compressed reducing the time Phobos spends in the tail.

In terms of modeling the Mars plasma environment, we are running plasma codes in sequence that apply from the largest scale across the inner heliosphere down to sizes of

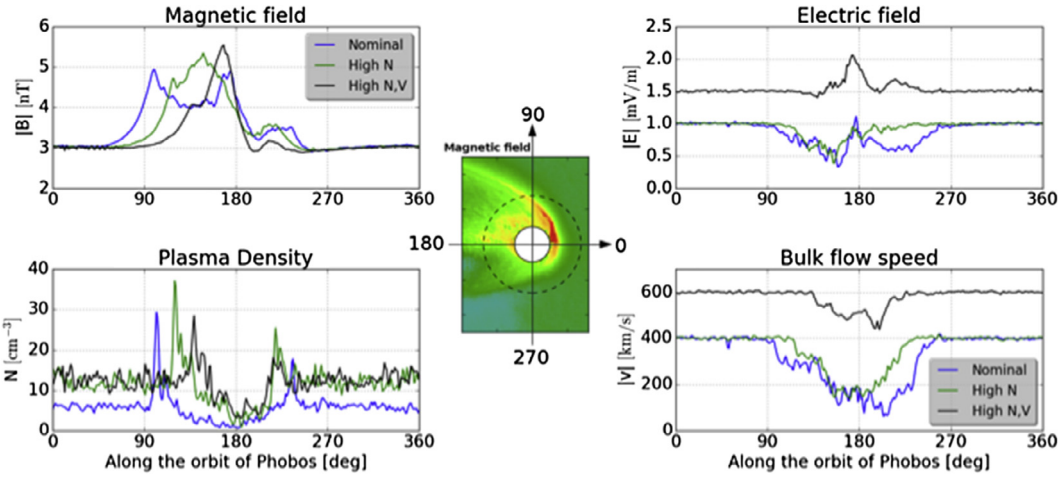

Fig. 5. Results from the hybrid simulation of the near-Mars plasma environment along Phobos' orbital path. Shown are the magnetic field, plasma density, electric field, and bulk flow speed for nominal solar wind and disturbed solar wind. The disturbed cases include higher solar wind density and higher overall solar wind flux. In the figure, 0° is at noon local time and 180° is in at midnight local time. Note that the moon passes from solar wind (0° to 100°), to post-shocked high density magnetosheath solar wind (100−~110°), to lower density magneto-tail oxygen flow (~110° to 180°). The moon then moves back through the sheath (near 240°) and out in the solar wind (>270°). Crustal magnetic fields are included in the model, based on Cain et al., 2003.

about 0.1 m in addressing astronaut boot charging (Section 6). Specifically, Fig. 4 shows a CME moving through the inner heliosphere in a display having a size of ~2 AU or three hundred million kilometers. Figs. 3 and 5 used a hybrid ion-electron code that shows the effects of such a large storm on the Mars system on scales of ~5 Martian radii (~15,000 km), but does not have the resolution to include the small moon. In the next section we then present plasma kinetic analytical modeling of the plasma interaction with the exposed body Phobos, applicable at scale sizes of a few kilometers (with resolution at sub-kilometer scales). Such kinetic modeling of ambipolar processes at sub-kilometer scales cannot be properly incorporated into regional-scale hybrid codes. We then apply the modeled near-surface plasma environment from the ambipolar code to examine astronaut charging and discharging on meter scales – with the plasma character as inputs to a dynamic differential equation of astronaut boot charging. We thus run these codes in sequence from large-to-small scale, using the character of the results (or the results themselves) from the larger scale code as an input to the code at the smaller scale. We are in fact contextually applying 4 models covering the plasma interaction on spatial scales that extend over twelve orders of magnitude: From 2 AU or $\sim 3 \times 10^{11}$ m and hierarchically mapping effects down to an astronaut boot surface at ~0.1 m.

4. The ambipolar expansion of plasma into shadowed regions

The plasma ambipolar expansion formalism that describes the plasma inflow into shadowed and obstructed regions has been previously described in Farrell et al. (2010) and Zimmerman et al. (2013). Specifically, immediately behind an obstruction to a plasma flow, a plasma void forms. Fig. 2 illustrates the geometry for the solar wind flowing behind an obstruction at a terminator region of an airless body (in the figure, an exposed crater wall). The solar wind is initially flowing in the x-direction, and the distance downstream from the obstacle is Δx. Along connecting magnetic field lines, electrons move into the void ahead of the ions and an ambipolar E-field forms that acts to deflect & accelerate the ions vertically along Δz into regions behind the obstruction. The ambipolar potential that develops into the trailing void has the form (Crow et al., 1975; Samir et al., 1983; Halekas et al., 2005)

$$e\phi_A/kT_e = -1.08(z'/t') - 1 \quad (1)$$

where the plasma is expanding into distance z' defined as the normalized distance from the plasma-void edge into the void, $\Delta z/\lambda_D$, and t' is the normalized time of the expansion from the point of obstruction, $\omega_{pi}t$. The variable λ_D is the plasma Debye length and ω_{pi} is the ion plasma frequency. As indicated in Fig. 2, Δz is the distance from the plasma-void edge into the void. At $t' = 0$, the plasma void is formed and the plasma discontinuity is in the form of a perfect step function located at $z' = \Delta z = 0$ (exactly along the wake flank). As time evolves, the plasma convects downstream with fluid elements located at position Δx (t') relative to the obstruction point. At location Δx, the plasma has also expanded inward defined by z' with the plasma inflow now located as position $\Delta z(t')$ into the void. For a time stationary wake, the time t' corresponds to a specific distance that a plasma fluid element has convected downstream from the obstacle, such that $t' = \Delta x\ \omega_{pi}/V_{sw}$ with the downstream distance, Δx, being the horizontal distance from the edge of the obstruction (see Fig. 2). Consequently, the time-stationary ambipolar potential trailing behind an obstruction in the solar wind can be re-expressed as (Farrell et al., 2010)

$$e\phi_A(\Delta x,\Delta z)/kT_e = -(V_{sw}\Delta z/C_s\Delta x) - 1 \quad (2)$$

where C_s is the ion sound speed ($=\lambda_D\omega_{pi}$). Typically, $V_{sw}/C_s \sim 10$.

As an illustrative example, consider a case where the observer is 20 km downstream from an obstruction point ($\Delta x = 20$ km) and 10 km inside of the plasma void ($\Delta z = 10$ km from the plasma-void edge). We would then expect the ambipolar potential at this location to be approximate $e\phi_A \sim -6\,kT_e$ or 6 times the electron temperature (in units of eV). For a solar wind electron temperature near 10 eV, this would correspond to a local ambipolar potential of ~−60 V.

The ambipolar E-field forms maintain neutrality and retard the electrons from inflowing into the void ahead of the ions. The plasma density at any (Δx, Δz) location in the void is $n(\Delta x, \Delta z) = n_o \exp(e\phi_A(\Delta x, \Delta z)/kT_e)$, where n_o is the density of the unobstructed plasma flow (Samir et al., 1983; Halekas et al., 2005; Farrell et al., 2010).

For the obstructed solar wind like that in Fig. 2, we can derive the current inflowing into the void from the point of obstruction as (Farrell et al., 2010):

$$J_e \sim n_{eo} e v_{te} \exp(e\phi_A/kT_e)(1 - \delta_{eff}) \tag{3a}$$

$$J_{iz} \sim -n_{eo} e(((\Delta z/\Delta x)V_{sw} + C_s) + V_{sw}\mathrm{Sin}(\theta_{sw})) \times \exp(e\phi_A/kT_e) \tag{3b}$$

$$J_{ix} \sim n_{eo} e V_{sw} \mathrm{Cos}(\theta_{sw}) \exp(e\phi_A/kT_e) \tag{3c}$$

where θ_{sw} includes the effect of a solar wind flow that is inflowing tilted at an angle relative to the x direction and v_{te} is the electron thermal velocity. For perfectly horizontal flowing solar wind, $\theta_{sw} = 0°$. We also include the effect of secondary electrons emitted from the surface in shadow (e.g., at the bottom of the crater floor) by adding a δ_{eff} to the electron thermal flux.

For a horizontal flowing solar wind ($\theta_{sw} = 0°$) impeded by an obstacle, the formalism above can be simplified to obtain an expression for the ambipolar ion influx behind the obstacle. Specifically, for locations with $V_{sw}\Delta z/C_s\Delta x > 1$ (or for $V_{sw}/C_s \sim 10$, $\Delta z/\Delta x > 0.1$) and obstacle size greater than a plasma Debye length, the obstructed ion influx can be approximated by the formula:

$$\mathbf{F}(\Delta x,\Delta z) \sim F_o \exp(-V_{sw}\Delta z/C_s\Delta x)\left(1\mathbf{x} + \frac{\Delta z}{\Delta x}\mathbf{z}\right) \tag{4a}$$

having a magnitude of

$$F(\Delta x,\Delta z) \sim F_o\left(1 + \left(\frac{\Delta z}{\Delta x}\right)^2\right)^{1/2} \exp(-V_{sw}\Delta z/C_s\Delta x) \tag{4b}$$

where F_o is $n_{eo}V_{sw}$ (nominally at $2 \times 10^{12}/m^2$-s for typical solar wind).

For example, consider the case where $V_{sw} = 450$ km/s, $C_s = 45$ km/s, and the observation point is located downstream by $\Delta x = 2$ obstacle radii and located inside the plasma void/wake region at $\Delta z = 1$ obstacle radius. The ion flux at this location (Δx, Δz) = (2, 1) is reduced by $F/F_o \sim 7 \times 10^{-3}$. Given the formula above, the ion influx at locations about an obstacle can be calculated and mapped out, in a general way.

For an obstacle like a lunar polar crater shown in Fig. 2, Eqs. (3 and 4) apply at locations in free space behind the obstacle. However, as this obstructed plasma flow approaches the shadowed surface behind the obstacle, the surface will develop a second electron-retarding potential as it forms its own surface-plasma sheath. This sheath forms to create flux balance at the surface itself. This second potential, the surface potential, ϕ_s, adds to the ambipolar potential, creating a total potential change relative to the undisturbed solar wind as $\Delta\phi = \phi_A + \phi_S$.

The surface potential, ϕ_S, is calculated assuming current balance at the surface in a local thin-sheath planar geometry:

$$J_e \exp(e\phi_S/kT_e) - |J_i|\mathrm{Sin}(\theta_{flow} - \theta_{topo}) = 0 \tag{5}$$

where J_e and J_i are the ambipolar-altered electron and ion current flux from Eq. (3) and θ_{topo} is the elevation angle of the local surface.

There are indeed locations along the floor behind the obstruction where ions cannot reach the surface because the difference in ion flow and topographic angles exceeds 90°. At these locations, the quasi-isotropic electrons are incident with the surface but the directed ion flow does not allow ions to be incident on the tilted surface. A local electron cloud develops. Particle-in-cell codes (Zimmerman et al., 2011, 2013) indicate that anomalously large negative surface potentials and E-fields develop at such locations that further divert the ion flow into the electron cloud region. We do not explicitly model these local topographic electron clouds along the floor of the shadowed region but do identify the locations where ions cannot propagate and where such anomalous local E-fields should develop.

Halekas et al. (2005) found that the apparent morphology of the expansion appears similar whether the IMF is quasi-parallel or quasi-perpendicular to the local wake flank (there are changes in ion inflow speed and direction that are IMF controlled). We note that the size of Phobos is comparable to an electron gyro-radius but smaller than a proton gyro-radius, and thus we can treat the ions as unmagnetized. The electrons are required to be magnetically connected from the solar wind to the surface, and in our calculations below we assume the ambient B field is directed primarily along Δz (parallel to the E-field direction). The protons flowing along Δx will then be deflected by the ambipolar potential that forms in the void region.

5. Ambipolar expansion and surface charging at Phobos near Stickney crater

The analytical formalism from Eqs. (1-5) was coded with the ambipolar potential, plasma flux, and surface potential all calculated from obstacle locations identified from a topographic surface map. This method was initially applied to the lunar south polar topography to examine the ambipolar expansion of plasma into permanently shad-

owed polar craters during both solar wind nominal and solar storm time conditions (Farrell et al., 2010; Jackson et al., 2011; Zimmerman et al, 2013). The code was later updated using LRO laser altimeter-derived topographic information and to allow for the input of dynamic solar wind conditions.

Herein, we describe a new application of the ambipolar expansion code to Phobos, using the M1 Phobos shape model/topographic data set maintained in the Planetary Data System (PDS) and described in Thomas (1993). The PDS link is http://sbn.psi.edu/pds/resource/oshape.html. We especially examined the plasma-surface interaction in a region near Stickney crater; therein considering the surface and near-moon environment where negative potentials develop due to the ambipolar inflow of the moon-obstructed plasma. Stickney crater is a location of topographic extremes making it ideal to examine plasma inflow to the crater floor. We consider times when the moon is located upstream of Mars, immersed in both nominal and disturbed solar wind. We also model times when the moon is in the Martian magnetic tail.

Fig. 6a shows the ambipolar potential that develops in downstream regions about Stickney Crater and the Mars-facing surface of the moon for a location of the moon at 10 h local time (located sunward of Mars, in the unperturbed solar wind flow). We apply Eq. (2) that describes the ambipolar potential in regions about an obstacle. At this specific local time, the moon is angled such that the anti-sunward-directed solar wind flows nearly horizontal overtop Stickney crater. We apply nominal MAVEN-measured solar wind conditions at 2.4 cm^{-3}, 370 km/s flow speeds and electron and ion temperatures of 7.5 eV and 5.5 eV, respectively.

As evident in the figure, large negative potentials develop in the region within Stickney crater. The region above the Mars-facing surface of Phobos also has obstructed solar wind, and thus a trailing ambipolar potential (wake) develops, with potentials below – 100 V in the trailing plasma. These events are similar to the wake that develops behind the our own Moon in the solar wind.

The associated topography is shown in Fig. 6b. To create this profile, we defined a slice about Phobos (in this case, one encircling the moon's equator) and intercepted it with a line (the x-axis) that is directed parallel to the solar wind flow but also cuts through the center of the moon. The z-axis is then the perpendicular distance from a specific point along x to the surface at the great circle. This construction shown in Fig. 6b shows the (x, z) topographic profile that the solar wind has to flow over and expand into.

Fig. 6**c** shows the surface and ambipolar potential calculated using Eqs. (3) and (5) for the topography shown in

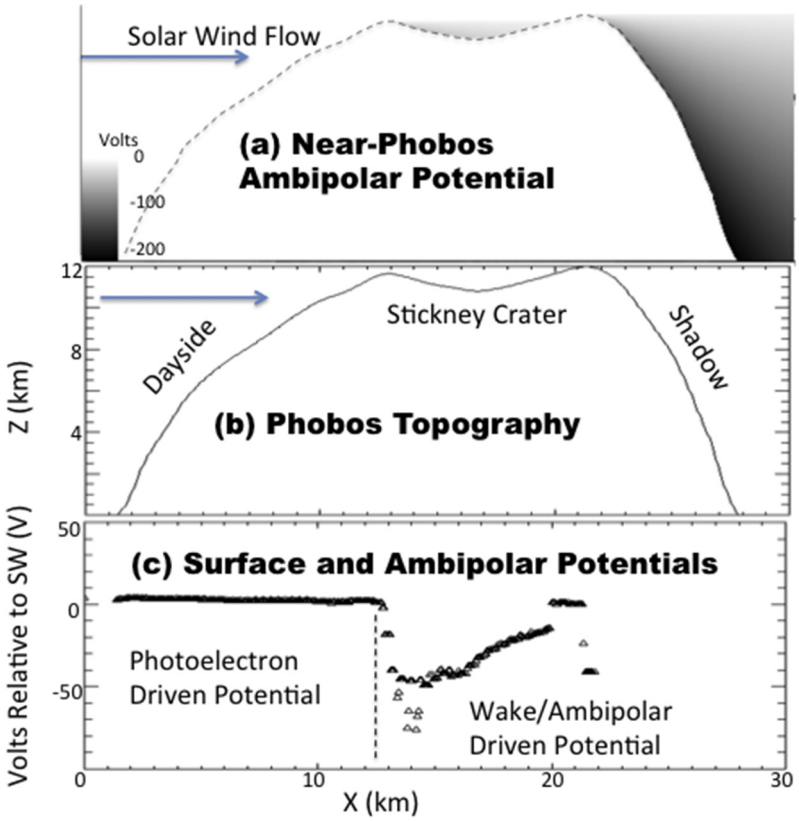

Fig. 6. The modeled ambipolar region in the trailing solar wind void/wake at Phobos, for the moon located at 10 h LT in nominal solar wind flow. Shown are the (a) near-moon wake potentials, (b) the moon topography, and (c) the total potential relative to the undisturbed solar wind at the surface. We apply a solar wind density of 2.4 cm^{-3}, 370 km/s flow speeds and electron and ion temperatures of 7.5 eV and 5.5 eV, respectively.

Fig. 6b. Within Stickney crater we find potentials can be at or below −40 V relative to the plasma potential in the unobstructed solar wind passing overhead, with the lowest potentials occurring on the crater wall along the leeward edge of the flow, where ion flux is the least. Within the crater, the surface potentials progressively increase away from this leeward edge in association with lower E-fields and reduced deflection. We note that the low plasma densities will increase the near-surface sheath size possibly to the size of the crater itself. Consequently, the sheath and ambipolar potentials may merge into one large region, similar to the merged sheath and ambipolar region trailing a small asteroid (see Figure 3 and 6 of Zimmerman et al., 2014).

We also note that we cannot derive a surface potential, ϕ_S, on the Mars-facing side of the moon ($x > 22$ km) using the simple form in Eq. (5). The unusual topography of the moon does not allow the solar wind ions to be directly incident at this surface. The large radius of curvature along this Mars-facing surface eastward of Stickney crater makes the surface slope descend steeply and the solar wind ions cannot be electrostatically-deflected/diverted by the ambipolar fields (alone) to the required large perpendicular angles in such short downstream distances to allow ion incidence with this steeply faced surface. Along this face, we thus have the development of an electron cloud – a region devoid of ions to the near-surface.

Self-consistent particle-in-cell simulations of these electron cloud regions indicate that anomalously large surface potentials develop to repel the energetic tail of the distribution of inflowing electrons and attract ions (Zimmerman et al., 2011). Anomalously large E-fields that extend well beyond the local sheath form, and these extend into the region where ions are present in the near-space (see Figure 2b of Zimmerman et al., 2011). In some sense, at the electron cloud-surface interaction region, the sheath is dynamically altered, with the large negative surface charge acting to repel the electrons, lowering the local electron content, and in turn, increasing the size of the Debye sheath. According to the self-consistent simulations, the size of the sheath increases and merges into the ambipolar region until the surface-connected E-fields reach locations where the needed ions are present - to further divert the ion flow towards the ion-depleted electron cloud region. A comparison of Zimmerman's et al.'s (2011) Fig. 2a–c shows this increased ion deflection in association with greatly enhanced surface E-fields. We do not include the particle-in-cell results herein, since they represent a nonlinear process that is not captured in our simpler model. However, we do note that the surface potential is not fully determined via Eq. (5) alone and we thus identify the region as anomalous.

Fig. 7 has the same format as Fig. 6, but now for Phobos immersed in plasma from a solar storm in its position at 10 h local time, like the storm passing Mars on 8 March 2015 (Jakosky et al., 2015a). We apply Maven-measured solar storm conditions having a density of 2.7 cm^{-3}, a solar wind flow speed of 832 km/s and electron and ion temperatures of 33 eV and 88 eV, respectively. These values correspond to the warm sheath region of the passing interplanetary shock that precedes the dense CME driver gas.

As evident in the figure, the surface potentials have greatly increased, by about a factor of 4, over non-storm time periods. Since the negative surface potential varies approximately as T_e, the factor of four increase in surface potential is related to the increase in plasma electron temperature from 7.5 eV in nominal times to 33 eV in disturbed conditions. Fig. 7c indicates that a closed solution is obtained to the surface potential on the Mars-facing side ($x > 22$ km), with values exceeding −600 V at the anti-solar point. In this case, a current balance solution is found on the Mars-facing surface due to the greater emission of surface-emitted secondary electrons induced from the warmer primary electron population. The higher yield of the secondary component (with yield varying as T_e) now creates outward electron emission necessary to bring the surface into equilibrium. The equilibrium is created mostly between primary and secondary electron components, with ion inflow still limited.

Fig. 8 also has the same format as Figs. 6 and 7, now showing the ambipolar potential (Fig. 8a) and surface potential (Fig. 8c) for Phobos in the Martian magnetic tail, located at 22 h local time on the Martian nightside. Oxygen-rich plasma originating from Mars is flowing past the moon (from left to right) and incident on the Mars-facing surface (which lies at $0 < x < 9$ km). The code was modified to include the larger mass of oxygen in the tail, which reduces the ion sound speed and hence the ratio of V_{sw}/C_s in Equations (2−4). In this case, we use the plasma parameters shown in Fig. 3 in the tail region from the hybrid simulation as input to the ambipolar code. The nominal tail plasma has a density of 0.5 cm^{-3}, a flow speed of 300 km/s, and electron temperatures ~20 eV.

Fig. 8a shows the development of a substantial ambipolar region forming behind the moon in the trailing plasma void/wake, with negative values below −200 V forming deep in the shadowed regions. Fig. 8c shows that large negative surface potentials from both within Stickney crater and on the anti-Mars side of the moon. Within Stickney crater, the largest negative potentials are again located on the crater wall along the leeward edge of the flow, in locations where ions have difficulty accessing. We note that the topography in shadowed locations beyond $x > 18$ km has a relatively small radius of curvature and is not steeply descending in z-value – thereby allowing a determination of the surface potential via Eq. (5).

6. Astronaut charging at Phobos

As an astronaut transits over a surface, they will develop charge via contact electrification (or tribocharging) between the astronaut boot and the regolith (Farrell et al., 2010; Jackson et al., 2011). This tribo-charge buildup is dissipated by the local plasma currents. For environmen-

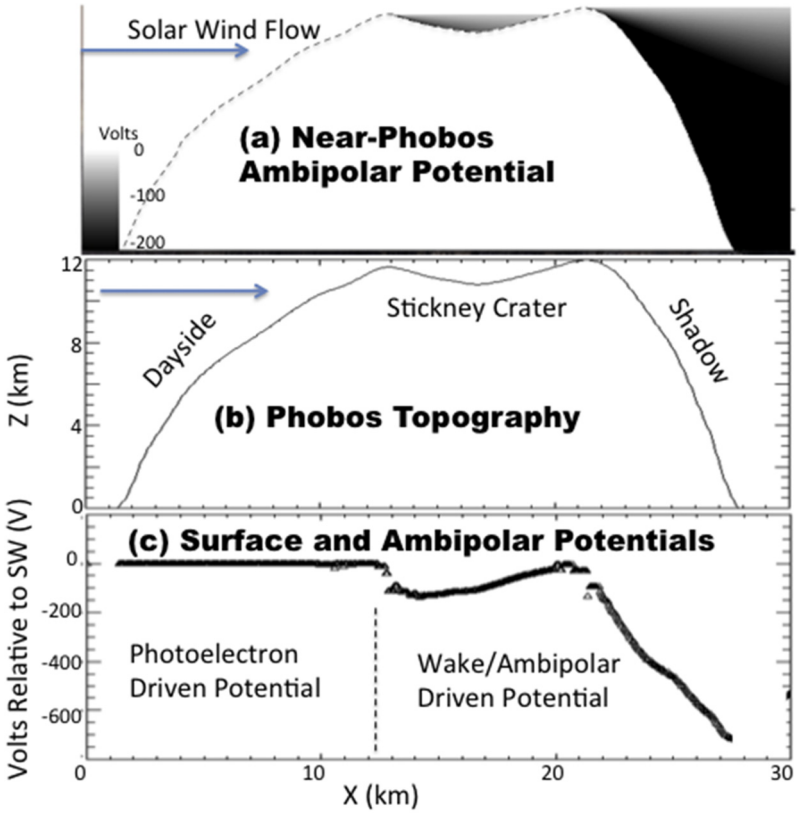

Fig. 7. The modeled ambipolar region in the trailing solar wind void/wake at Phobos, for the moon located at 10 h LT in disturbed solar wind flow associated with the warm plasma just behind the passing interplanetary shock (driven by the CME). Shown are the (a) near-moon wake potentials, (b) the moon topography and (c) the total potential relative to the undisturbed solar wind at the surface. We apply conditions with a plasma density of 2.7 cm^{-3}, a solar wind flow speed of 832 km/s and electron and ion temperatures of 33 eV and 88 eV, respectively.

tal currents in exposed daylight, the local current density can be as large as a few $\mu A/m^2$ (see Table 1 of Jackson et al., 2015) which can easily off-set mild tribo-charging. For example, triboelectric charging was easily dissipated on the lunar dayside during the Apollo missions. There was enough environmental plasma to remediate any charge build-up.

However, in shadowed locations, like within Stickney crater when Phobos is at 10 h LT (Fig. 6), the environmental plasma currents along the crater floor are reduced by nearly ~10,000 compared to topside regions due to the formation of the crater obstacle void and ambipolar low density plasma expansion. In this case, tribo-electric charging currents on the astronaut boot may exceed plasma dissipation currents leading to anomalous charge build-up during roving along the shadowed crater floor (Jackson et al., 2011). For demonstration, we use a boot as a contact point with the regolith, but in the low gravity environment of Phobos, an astronaut may make contact via a gloved hand while attached to an anchored platform. The charging effect is the same in either case.

To consider this charging-discharging effect, we have to create a functional form for a tribo-electric source term. If we assume a boot has a 10 cm × 10 cm area in contact with the surface, and that surface consists of a bed of 100 μm grains, then at each contact, there are approximately $N = 10^6$ grains in contact with the boot. The charge transfer per grain, in a scaled form, has been derived previously as (Desch and Cuzzi, 2000):

$$\Delta q = (\Delta\Phi/2V)(r_g/0.5\ \mu m)0.4\ fC \quad (6)$$

with $\Delta\Phi$ being the tribo-electric potential difference between the astronaut boot material and the regolith. Typically, the tribo-electric potential has values similar to a material's work function. Hence, when material have similar compositions, the tribo-electric potential difference is relatively small ($\Delta\Phi$ ~0.02 V) and there is a small amount of charge exchanged. In contrast, when compositions vary greatly (like metals and insulators, $\Delta\Phi$ ~2 V) the charge exchange is great. Ironically, the Apollo space suit material consisted of woven Teflon. Teflon is an extreme tribo-electricially negative material and will charge strongly negative when in contact with most other materials (like lunar regolith).

Given this formalism, the tribo-electric source term, S, becomes

$$S = N\Delta q\delta(t - n\Delta t)\ \ n = 0, 1, 2, 3, \ldots. \quad (7)$$

where $n\Delta t$ represents the repeated impulsive contact of the astronaut boot with the surface, with contacts temporally-

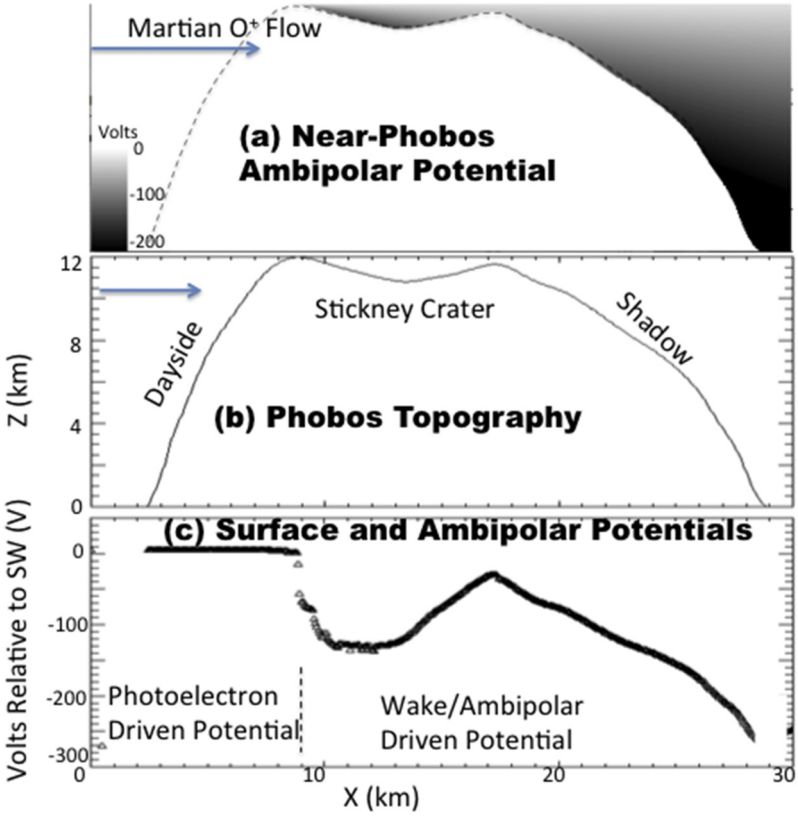

Fig. 8. The modeled ambipolar region in the trailing void/wake at Phobos fromed by the flowing oxygen ions from Mars, for the moon located at 22 h LT. Shown are the (a) near-moon wake potentials, (b) the moon topography, and (c) the total potential relative to the undisturbed plasma. We apply a Mars Oxygen-rich tail density of 0.5 cm^{-3}, a flow speed of 300 km/s, and electron temperatures ~20 eV.

spaced at intervals Δt. For example, an astronaut boot might be in repeated contact with the surface every 2 seconds as defined by the astronaut's stride.

Consider the following: for a boot/regolith tribo-electric potential difference of $\Delta\Phi = -0.2$ V and $r_g = 50$ μm, the total charge transferred from grain to boot is $S = -4$ nC per contact. The dissipation time to remove this charge is approximately $T = S/I_{env}$, where current $I_{env} = J_{env}\ A_{boot}$, J_{env} being the local environmental plasma current density in the region, $A_{boot} = 0.01\ m^2$ being the boot area.

As a simple example, let us consider a boot charging negatively at each step to −4 nC, and an astronaut walking at a cadence of $\Delta t = 5$ s per step. If the positive ion current density in the region is ~1 $\mu A/m^2$ (like on the dayside solar wind ion flow), then it takes only $T = 0.4$ s to remediate any tribo-charge build-up on the 10 cm × 10 cm area. At this time scale, there is nearly complete dissipation of this boot charge between each astronaut step (at 5 s intervals). There is no net charge build-up. However, if in shadowed regions, the ion current levels drop to 0.1 nA/m^2, then the dissipation time is ~4000 seconds. Charge cannot dissipate between steps, accumulating to anomalously large levels during the traverse.

Fig. 9 shows the ambipolar model-derived ion and electron near-surface currents in the Stickney crater region while Phobos is at 10 h LT under nominal solar wind conditions (currents are those from the same run to obtain Fig. 6). Topside of the crater, the ion currents are above 10^{-7} A/m^2, but decreases to near 10^{-10} A/m^2 within the ambipolar region that forms within the crater between 13 km < x < 16 km. The solar wind electron thermal flux is near 10^{-6} A/m^2 but decreases by nearly a factor of 10000 to 10^{-10} A/m^2 in the ambipolar region within Stickney Crater.

Using these currents between 13 km < x < 16 km along the crater floor, we can determine the dynamic charging of the astronaut by solving (Jackson et al., 2011)

$$C d\phi_{ast}/dt = J_e A(1-\gamma_{obj})\exp(e\phi_{ast}/kT_e) - J_i A/2 + J_s A\ \exp(e\phi_{ast}/kT_s) - C\phi_{ast}/t_r + S\ \exp(-t/t_a) \quad (8)$$

where C is the capacitance of the boot, ϕ_{ast} is the astronaut potential (a potential added to the ambipolar and surface potential to get the total potential drop from solar wind to astronaut), $J_{e,i,s}$ are the environment plasma electron thermal flux, plasma ion flow current, and surface-emitted low energy secondary electron currents, respectively, along the crater floor (from Fig. 9), and A is the boot area affected by charging. On the right hand side of the equation, the first two terms represent the dissipating plasma currents in the case of a negatively charge area.

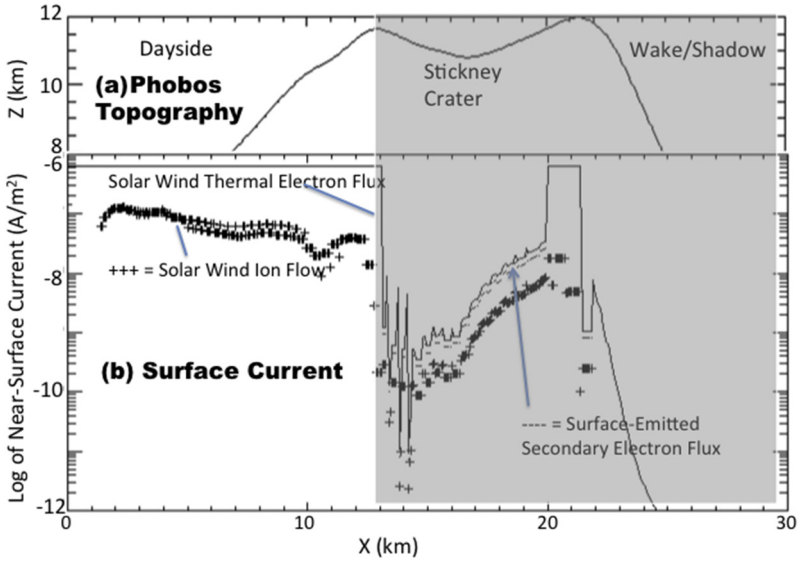

Fig. 9. The surface currents in the Stickney region for Phobos at 10 h LT in nominal solar wind flow (the currents associated with Fig. 6).

The third term represents direct dissipation of charge to the moon's regolith surface. If we assume that Phobos' shadowed cold regolith behaves electrically-similar to that at the Earth's Moon, the charge leakage times into the regolith, t_r, will be large (Carrier et al., 1991; Jackson et al., 2011), making this term insignificant. As described in Carrier et al. (1991), lunar silica-rich regolith is a semiconductor and the conductivity is a strong function of temperature – being as low as 10^{-16} S/m in cold locations near 100 K, making dissipation times into the regolith on the order of many days (Jordan et al., 2015). We assume that the dissipation to the plasma occurs faster than dissipation to the regolith. However, the time scale of plasma dissipation in shadowed regions may still be slow compared to faster human operations like walking or wheel roving, which charge on time-scales of seconds.

The last term in the expression is the tribo-electric source term, Eq. (7), but now modulated by a exponential decay, $\exp(-t/t_a)$. This temporal decay factor is the recognition that the tribo-electric generator will not remain perfectly efficient. Over time, t_a, the boot will itself become regolith-encrusted either via regolith cohesion or regolith electrostatic forces. As the boot becomes regolith encrusted, the tribo-electric efficiency will decay as the boot-regolith interface transforms into a regolith-regolith interface. The value of t_a is arbitrary but the term is required since charge build-up would continue infinitely otherwise. We thus expect that as the boot becomes regolith encrusted that the tribo-electric charging would self-diminish.

Fig. 10 shows the charging of an astronaut's boot as they walk along the shadowed Stickney crater floor with current environment like that in shown in Fig. 9 near x = 14 km. Displayed is the charging for three different boot/regolith contact potential differences, $\Delta\Phi =$ (a) 0.02 V, (b) 0.2 V, and (c) 2 V, for a bed of 100 μm diameter grains in contact with the 10 cm × 10 cm surface. We also show the equilibrium potential (of about −10 V) in a case when the astronaut is simply standing still and there is no tribocharging source. We assume that the tribo-electric efficiency due to regolith contamination of the surface is degraded on a $t_a \sim 20$ second time scale. The currents applied are those near X = 14 km in Fig. 9 with values of $J_e = 3.6 \times 10^{-10}$ A/m^2, $J_i = 8.6 \times 10^{-11}$ A/m^2, and $T_e = 7.5$ eV. The low energy secondary electron current emitted from the surface is $J_s = 2.7 \times 10^{-10}$ A/m^2. We also assume a secondary electron emission from the astronaut as well, at a yield of 0.5 of the primary J_e.

We note that if the boot were Teflon, then ΔΦ would be large, with tribo-charging expected between 1 and 10 kV over a minute of roving in the shadowed crater region. We thus recommend that the boot/regolith surfaces have similar tribo-potentials/work functions to reduce the tribo-electric charge generation (reduce S, the source term) (Jackson et al., 2011).

Fig. 11 shows the same charging situation but now with a disturbed solar wind plasma in the shadowed crater (Fig. 7). In this disturbed case, the current values applied are $J_e = 8 \times 10^{-9}$ A/m^2, $J_i = 1.7 \times 10^{-10}$ A/m^2, $J_s = 2.6 - \times 10^{-8}$ A/m^2 and $T_e = 33$ eV. Like in Fig. 10, the tribo-charging source term dominates the plasma dissipative losses in the early roving period and for material that differs substantially in contact potential, substantial charging is found to occur. We do note that the equilibrium potential (non-roving case) is larger than in Fig. 10 due, in part, to the larger electron temperature.

We note that the model herein determines surface charging using the ambient cold and warm plasma. It does not include effects from low intensity currents from high energy particle streams from solar energetic particles or galactic cosmic rays. In cooler regions such currents may lead to deep dielectric discharge and impulsive surface plasma

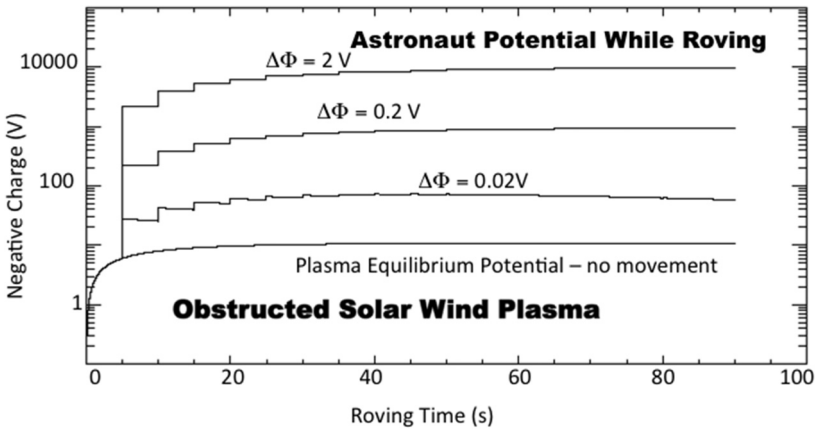

Fig. 10. Given the environmental electron and ion currents in Fig. 9 for a location deep in Stickney crater (X = 14 km), we determine the charge build-up for an astronaut walking over the surface, with charge generated via contact electrification. Note that deep in the crater, the environmental plasma currents are not large enough to offset the charge buildup.

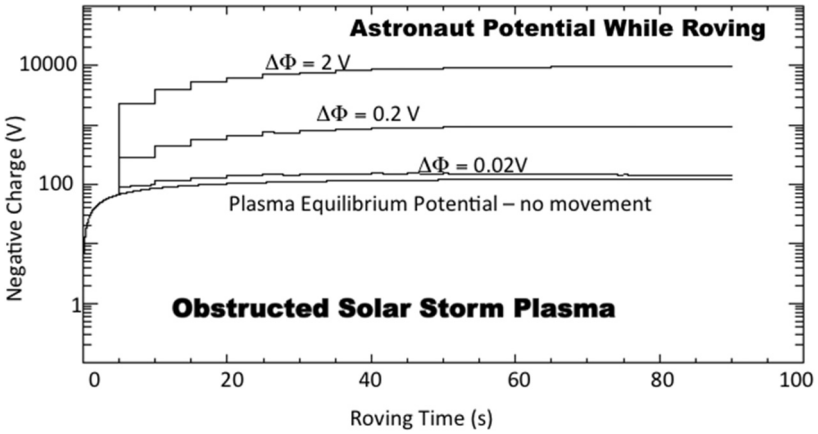

Fig. 11. That same as Fig. 10 but now using the local plasma currents for the passing CME post-shocked plasma that enter into the crater regions (e.g., Fig. 7).

release (Jordan et al., 2015). Recent simulations (Zimmerman et al., 2016) reveal that very large E-fields can develop between adjacent grains due to differential charging at micron-sized scales, and these may reflect protons off the surfaces of airless bodies. However, at the scale size of meters, these E-fields average to the surface potential. We do not consider these small sized E-fields in this analysis.

7. Discussion

As described in Section 5, in the case of nominal solar wind flow past the moon located at 10 h LT relative to Mars, we find the possible formation of an electron cloud region in the Mars-facing (shadowed) side of the moon (i.e., Fig. 6). Our simple calculations suggest that ions cannot be diverted/deflected to large enough angles in the ambipolar E-field to be incident with this very steep (large $\Delta z/\Delta x$) surface topography. The implications are that roving operations on this Mars-facing side, when in shadow, should be limited since there is little/no ion current available near the surface to offset any negative tribo-charge buildup. Note in Eq. (8) that if J_i is set to zero, dissipation into the surface regolith is the only means to discharge any negative charge build-up, and this trickle current may be too slow for any normal human activity.

In order to fully understand ion trajectories along this Mars-facing side, we suggest to run a particle-in-cell simulation that can then track the development of the anomalous, inflated sheaths that will likely develop that further deflects and draws ions to the local surface (as described in Section 5).

We also note that in all of our expansion calculations, we have assumed that the electron distribution is an isothermal Maxwellian distribution. Consequently, the electron temperature is constant throughout the expansion region. However, as pointed out in Halekas et al. (2005), the solar wind can be better-described as a non-isothermal kappa distribution, with the electron temperature increasing with increasing electron energy $T_e = T_e(U)$. Thus, in the ambipolar E-field, as low energy electrons in the core of the distribution are repelled from the inflowing

population, a warmer, less dense population of higher energy electrons remain. The ambipolar E-field effectively filters the solar wind electron distribution as a function of its energy, but also filters in electron temperature as well. At the anti-solar location deep in the wake, the electron temperature of the energy-filtered distribution can be 5–10 times higher than nominal levels (Figure 12 of Halekas et al., 2005) when considering a kappa distribution.

Thus, for a non-isothermal warmer electron distribution (non-Maxwellian) incident at the shadowed surface of Phobos, we would expect higher yields of secondary electrons compared to the Maxwellian, since such yields vary directly with T_e. This higher level of secondary electrons current will also act to bring the surface into current balance (like it does in Fig. 7), with the equilibrium surface potential forcing J_e to be equal to J_s. Since we model Maxwellian distributions, we do not incorporate this non-isothermal effect. Redoing the analysis for a kappa distribution will be a focus of future work.

Fig. 10 indicates that an astronaut's boot can become charged to very large potential values. In doing so, local electrostatic forces originating from the astronaut may accelerate grains towards the astronaut. Once on the astronaut, the grains would become further entrenched via inter-atomic cohesion forces and/or mechanical forces. In the former, molecular-level Van der Waal forces between the surface of the astronaut boot and grain creates strong grain attraction or sticking. In essence, atoms of the grain are trapped in the inter-atomic potentials of the atoms residing along the outer-most layer of the boot material (Hartzell and Scheeres, 2011). In the latter, the irregularly-shaped sharp surfaces of the grain hook themselves into the fabric of the astronaut boot. Such was the case for the Apollo space suits (Christoffersen et al., 2009). A comparison of these forces will be presented in another paper in this special issue by Hartzell et al. (2018).

8. Conclusions

Using an ambipolar diffusion code, we present a new mapping of the near surface and surface electrostatic potentials that likely develop at Mars' moon Phobos. We demonstrate that large potentials can develop within shadow crater regions, like within Stickney crater when Phobos is located at 10 h local time relative to Mars. We also demonstrate that large ambipolar potentials develop on the Mars-facing side of the Moon – with the possible formation of an ion- sparse electron cloud region.

During the passage of a coronal mass ejection, like the one on 8 March 2015, we find the development of even larger electrostatic potentials (~4 times larger) both within Stickney crater and on the Mars facing side of the moon.

We also derive an impact on human explorers of this near-moon plasma environment: In shadow regions, the local environmental currents drop to low levels, and fail to adequately provide needed charge dissipation to offset astronaut charging via contact electrification. We thus suggest that any explorer remain in contact with sunlit surfaces and that the space suit material have a material work function similar to that of the regolith – this to reduce tribo-electric charging. Missions have been proposed to collect and return samples of Phobos regolith material, and such samples should have their electrical properties tested, including characteristics such as conductivity with temperature, tribo-charging potential (i.e., the work function), and secondary electron yield. At this point, these regolith properties remain knowledge gaps and we rely almost exclusively on Apollo sample analogs to provide initial estimates of the grain properties.

Acknowledgements

The authors gratefully acknowledge support from NASA's Solar System Exploration Research Virtual Institute (SSERVI) in completion of this work.

References

Cain, J.C., Ferguson, B.B., Mozzoni, D., 2003. An n = 90 internal potential function of the Martian crustal magnetic field. J. Geophys. Res. 108 (E2), 5008. https://doi.org/10.1029/2000JE001487.

Carrier, W.D., Olhoeft, G.R., Mendell, W., 1991. Physical properties of the lunar surface. In: Heiken, G.H. et al. (Eds.), The Lunar Sourcebook. Cambridge Univ. Press, Cambridge, U.K., pp. 475–594.

Christoffersen, R., Lindsay, J.F., Noble, S.K., et al., 2009. Lunar dust effects on spacesuit systems: Insights from Apollo spacesuits, NASA/TP-2009-214786 <http://ntrs.nasa.gov/>.

Crow, J.E., Auer, P.L., Allen, J.E., 1975. The expansion of plasma into a vacuum. J. Plasma Phys. 14, 65–76. https://doi.org/10.1017/S0022377800025538.

Desch, S.J., Cuzzi, J.N., 2000. The generation of lightning in the solar nebula. Icarus 143, 87–105. https://doi.org/10.1006/icar.1999.6245.

Farrell, W.M., Stubbs, T.J., Halekas, J.S., Delory, G.T., Collier, M.R., Vondrak, R.R., Lin, R.P., 2008. Loss of solar wind plasma neutrality and affect on surface potentials near the lunar terminator and shadowed polar regions. Geophys. Res. Lett. 35, L05105. https://doi.org/10.1029/2007GL032653.

Farrell, W.M., Stubbs, T.J., Halekas, J.S., Killen, R.M., Delory, G.T., Collier, M.R., Vondrak, R.R., 2010. Anticipated electrical environment within permanently shadowed lunar craters. J. Geophys. Res. 115, E03004. https://doi.org/10.1029/2009JE003464.

Farrell, W.M., Poppe, A.R., Zimmerman, M.I., Halekas, J.S., Delory, G.T., Killen, R.M., 2013. The lunar photoelectron sheath: a change in trapping efficiency during a solar storm. J. Geophys. Res. Planets 118. https://doi.org/10.1002/jgre.20086.

Fraeman, A.A., Murchie, S.L., Arvidson, R.E., et al., 2014. Spectral absorptions on Phobos and Deimos in the visible/near infrared wavelengths and their compositional constraints. Icarus 229, 196–205.

Feuerbacher, B., Anderegg, M., Fitton, B., Laude, L.D., Willis, R.F., Grard, R.J.L., 1972. Photoemission from lunar surface fines and the lunar photoelectron sheath. Geochim. Cosmochim. Acta 3 (Suppl. 3), 2655–2663.

Halekas, J.S., Bale, S.D., Mitchell, D.L., Lin, R.P., 2005. Electrons and magnetic fields in the lunar plasma wake. J. Geophys. Res. 110, A07222. https://doi.org/10.1029/2004JA010991.

Halekas, J.S., Saito, Y., Delory, G.T., Farrell, W.M., 2011. New views of the lunar plasma environment. Planetary Space Sci. 59, 1681–1694.

Hartzell, C.M., Farrell, W.M., Marshall, J.R., 2018. Shaking as a means to detach adhered regolith for manned Phobos exploration. Adv. Space Res. 62, 2213–2219. https://doi.org/10.1016/j.asr.2017.09.010.

Hartzell, C.M., Sheeres, D.J., 2011. The role of cohesive forces in particle launching on the Moon and asteroids. Planetary Space Sci. 59, 1758–1768.

Jackson, T.L., Farrell, W.M., Zimmerman, M.I., 2015. Rover wheel charging on the lunar surface. Adv. Space Res. 55, 1710–1720. https://doi.org/10.1016/j.asr.2014.12.027.

Jackson, T.L., Farrell, W.M., Killen, R.M., et al., 2011. The discharging of roving objects in the lunar polar regions. J. Spacecr. Rock. 48, 700–703. https://doi.org/10.2514/51897.

Jakosky, B.M., Grebowsky, J.M., Luhmann, J.G., et al., 2015a. MAVEN observations of the response of Mars to an interplanetary coronal mass ejection. Science 350. https://doi.org/10.1126/science.aad0210.

Jakosky, B.M., Grebowsky, J.M., Luhmann, J.G., Brain, D.A., 2015b. Initial results from the MAVEN mission to Mars. Geophys. Res. Lett. 42, 8791–8802. https://doi.org/10.1002/2015GL065271.

Jakosky, B.M., Lin, R.P., Grebowsky, J.M., et al., 2015c. The Mars Atmosphere and Volatile Evolution (MAVEN) mission. Space Sci. Rev. 195, 3–48. https://doi.org/10.1007/s11214-015-0139-x.

Jordan, A.P., Stubbs, T.J., Wilson, J.K., Schwadron, N.A., Spence, H.E., 2015. Dielectric breakdown weath-ering of the Moon's polar regolith. J. Geophys. Res. Planets 120, 210–225. https://doi.org/10.1002/2014JE004710.

Manka, R.H., 1973. Plasma and potential at the lunar surface. In: Grard, R.J.L. (Ed.), Photon and Particle Interactions With Surfaces in Space. Reidel, Dordrecht, Netherlands, pp. 347–361.

Mays, M.L., Taktakishvili, A., Pulkkinen, A., et al., 2015. Ensemble modeling of CMEs using the WSA-ENLIL + Cone model. Sol. Phys. 290, 1775–1804. https://doi.org/10.1007/s11207-015-0692-1.

Ogilvie, K.W., Steinberg, J.T., Fitzenreiter, R.J., Owen, C.J., Lazarus, A. J., Farrell, W.M., Torbert, R.B., 1996. Observations of the lunar plasma wake from the wind spacecraft on December 27, 1994. Geophys. Res. Lett. 23, 1255–1258. https://doi.org/10.1029/96GL01069.

Poppe, A., Horányi, M., 2010. Simulations of the photoelectron sheath and dust levitation on the lunar surface. J. Geophys. Res. 115, A08106. https://doi.org/10.1029/2010JA015286.

Poppe, A.R., Curry, S.M., Fatemi, S., 2016. The Phobos neutral and ionized torus. J. Geophys. Res. Planets 121, 770–783. https://doi.org/10.1002/2015JE004948.

Samir, U., Wright Jr., K.H., Stone, N.H., 1983. The expansion of a plasma into a vacuum: basic phenomena and processes and applications to space plasma physics. Rev. Geophys. 21, 1631–1646. https://doi.org/10.1029/ RG021i007p01631.

Stubbs, T.J., Farrell, W.M., Halekas, J.S., et al., 2014. Dependence of lunar surface charging on solar wind conditions and solar radiation. Planetary Space Sci. 90, 10–27.

Thomas, P.C., 1993. Gravity, tides and topography on small satellites and asteroids: application to surface features of the Martian satellites. Icarus 105, 326–344.

Zakharov, A., Horanyi, M., Lee, P., Witasse, O., Cipriani, F., 2014. Dust at the Martian moons and in circummartian space. Planetary Space Sci. 102, 171–175.

Zimmerman, M.I., Farrell, W.M., Stubbs, T.J., et al., 2011. Solar wind access to lunar polar craters: Feedback between surface charging and plasma expansion. Geophys. Res. Lett. 38, L19202. https://doi.org/10.1029/2011GL048880.

Zimmerman, M.I., Jackson, T.L., Farrell, W.M., Stubbs, T.J., 2012. Plasma wake simulations and object charging in a shadowed lunar crater during a solar storm. J. Geophys. Res. 117, E00K03. https://doi.org/10.1029/2012JE004094.

Zimmerman, M.I., Farrell, W.M., Stubbs, T.J., 2013. Recursive plasma wake formation on the Moon and its effect on polar volatiles. Icarus 226, 992–998. https://doi.org/10.1016/j.icarus.2013.06.013.

Zimmerman, M.I., Farrell, W.M., Poppe, A.R., 2014. Grid-free 2D plasma simulation of the complex interaction between the solar wind and small, near-Earth asteroids. Icarusm 238, 77–85.

Zimmerman, M.I., Farrell, W.M., Hartzell, C.M., Wang, X., Horanyi, M., Hurley, D.M., Hibbitts, K., 2016. Grain-scale supercharging and breakdown on airless regoliths. J. Geophys. Res. Planets 121, 2150–2165. https://doi.org/10.1002/2016JE005049.